Two-scale topology optimization of macrostructure and porous microstructure composed of multiphase materials with distinct Poisson's ratios

Abstract

Negative Poisson's ratio (NPR) material attracts a lot of attentions for its unique mechanical properties. However, achieving NPR is at the expense of reducing Young's modulus. It has been observed that the composite stiffness can be enhanced when blending positive Poisson's ratio (PPR) material into NPR material. Based on the respective interpolation of Young's modulus and Poisson's ratio, two concurrent topology optimization problems with different types of constraints, called Problem A and B, are respectively discussed to explore the Poisson's ratio effect in porous microstructure. In Problem A, the volume constraints are respectively imposed on macro and micro structures; in Problem B, besides setting an upper bound on the total available base materials, the micro thermal insulation capability is considered as well. Besides considering the influence of micro thermal insulation capability on the optimized results in Problem B, the similar and dissimilar influences of Poisson's ratios, volume fractions in Problem A and B are also investigated through several 2D and 3D numerical examples. It is observed that the concurrent structural stiffness resulting from the mixture of PPR and NPR base materials can exceed the concurrent structural stiffness composed of any individual base material.

Keywords

Topology optimization, concurrent design, Poisson's ratio, multiphase materials

Jiao Jia[a, b]*
Wei Cheng[c]
Kai Long[d]

[a] Department of Automotive Engineering, School of Transportation Science and Engineering, Beihang University, Beijing 100191, China. E-mail: jiajiao_2012@163.com

[b] Advanced Vehicle Research Center (AVRC), Beihang University, Beijing 100191, China

[c] School of Aeronautic Science and Engineering, Beihang University, Beijing 100191, China. E-mail: cheng_wei@buaa.edu.cn

[d] State Key Laboratory for Alternate Electrical Power System with Renewable Energy Sources, North China Electric Power University, Beijing 102206, China. E-mail: longkai1978@163.com

* Corresponding author

1 INTRODUCTION

With a near 30-year development, the structural topology optimization has emerged a variety of approaches including homogenization method [Bendsøe and Kikuchi 1988], solid isotropic material with penalization (SIMP) method [Bendsøe 1989, Mlejnek 1992, Zhou and Rozvany 1991], evolutionary structural optimization (ESO) method [Xie and Steven 1993] and the updated version, bi-directional evolutionary structural optimization (BESO) method [Querin et al. 2000], level set method [Wang et al. 2003] and phase field method [Bourdin and Chambolle 2003]. Quite recently, an explicit topology optimization approach based on so-called moving morphable components (MMC) solution framework was presented by [Guo, Zhang, and Zhong 2014].

The concept of concurrent design can be traced to [Lakes 1993]. The pioneering work of [Rodrigues, Guedes, and Bendsoe 2002] was to introduce the topology optimization technique into concurrent design. However, any variable microstructure causes a high computational cost and manufacture difficulties. Later a more popular concurrent design method was developed by [Liu, Yan, and Cheng 2008]. In this method, uniform microstructure can be achieved which overcomes the issues mentioned above. During the optimization process, effective material properties are computed through the numerical homogenization technique and integrated into the analysis of macrostructure. Subsequently, a series of researches were carried out under this framework. [Yan, Cheng, and Liu

Jiao Jia et al.
Two-scale topology optimization of macrostructure and porous microstructure composed of multiphase materials with distinct
Poisson's ratios

2008] suggested that the structure composed of porous material has lower stiffness than the fully solid material structure. Moreover, [Niu, Yan, and Cheng 2009] also observed that the structure without porosity on micro-scale has higher fundamental frequency than the structure with porosity on micro-scale. A similar viewpoint is expressed in literature [Vicente et al. 2016]. Taken minimized frequency response as the objective, under the BESO framework, [Vicente et al. 2016] revealed that the fully solid material structure has a better result compared to the structure consisted of porous microstructure. The same conclusion can be obtained through porous microstructure converging to isotropic solid material under coupled volume constrains [Sivapuram, Dunning, and Kim 2016]. The above researches manifest that the structure made of porous material should consider the multifunctional demands. Basing on this idea, [Yan, Cheng, and Liu 2008], [Deng, Yan, and Cheng 2013], [Yan et al. 2014] and [Long, Wang, and Gu 2018] discussed the concurrent optimization of thermoelasticity and thermal conduction. Besides the discussion about the multifunctional applications, the concurrent approaches in considering multiphase materials are concerned as well in recent years. Especially Xu et al. [Xu, Jiang, and Xie 2015, Xu and Xie 2015, Xu et al. 2016] built the concurrent optimization models in regard to multiphase materials respectively under harmonic, random and mechanical-thermal coupled loads. [Da et al. 2017]) focused on the super multiphase materials problem in concurrent optimization. Besides the homogenization theory, other approaches are also employed in concurrent optimization. Basing on super element technique, [Zhang and Sun 2006] achieved the scale-related cellular materials and layered structures. [Yan, Hu, and Duan 2015] adopted extended multiscale finite element method to study the size-effect in concurrent structure which is composed of lattice materials. [Xia and Breitkopf 2014] introduced FE^2 model into concurrent optimization to solve the computational cost problem caused by multiscale nonlinearity.

Recent researches indicate that exceptional Poisson's ratios, e.g., Poisson's ratio towards to the thermodynamic limit 0.5, negative Poisson's ratio (NPR), are helpful to improve the composite stiffness, called as Poisson's ratio effect [Liu, Zhang, and Gao 2006, Lim 2010]. Moreover, when Young's moduli of the positive Poisson's ratio (PPR) and NPR base materials are close to each other, the maximum enhancement in stiffness is observed to happen with the PPR and NPR respectively approaching to the thermodynamic limits 0.5 and -1 [Kocer, McKenzie, and Bilek 2009]. Successive investigations validate that Poisson's ratio effect is influenced by Poisson's ratio, Young's modulus, dosages, shapes and distributions of base materials [Zuo and Xie 2014, Shufrin, Pasternak, and Dyskin 2015]. Young's modulus and Poisson's ratio are respectively interpolated for employing topology optimization technique to exploit Poisson's ratio effect in sandwich structured composites [Strek et al. 2014]. Besides maximizing the effective Young's modulus [Long et al. 2016], Long et al. [Long, Han, and Gu 2017, Long et al. 2018] extended the above model to reveal the Poisson's ratio effect in concurrent structure under volume fraction constraint and mass constraint.

In this paper, basing on the respective interpolation of Young's modulus and Poisson's ratio, Poisson's ratio effect in porous microstructure is revealed. Taken structural compliance as the objective, two optimization problems with different types of constraints, named as Problem A and B, are respectively discussed. In Problem A, the independent volume constraints are respectively imposed on macro and micro structures; in Problem B, besides setting an upper bound on the total available base materials, the thermal insulation capability in microstructure is also considered. The effective elasticity and thermal conductivity matrices obtained from the homogenization technique are respectively used in macro structural analysis and micro thermal insulation constraint. The remainder of the paper is organized as follows. Two concurrent optimization problems considering Poisson's ratio effect are established and described in Section 2. Section 3 provides the sensitivity analyses. The numerical implementation is given in Section 4. Section 5 presents several 2D and 3D numerical examples to illustrate the proposed models are effective to reveal the Poisson's ratio effect in concurrent optimization. Concluding remarks are given in Section 6.

2 CONCURRENT TOPOLOGY OPTIMIZATION PROBLEM WITH PPR AND NPR MATERIALS

Considering a two-scale system, as shown in Fig. 1, the macrostructure (Fig. 1(a)) is comprised of periodic materials (Fig. 1(b)) whose unit cell (Fig. 1(c)) is constituted by isotropic PPR and NPR base materials. The microstructure is assumed to be orthotropic. In Fig. 1(c), the PPR and NPR base materials are respectively represented by blue and red. P_i ($P_i \in [\delta, 1]$, i = 1, 2, ..., M, M is the total number of elements on macro-scale) is taken as the macro design variable, with representation of the relative density of the ith macro element. δ is a small predetermined value to avoid numerical singularity in optimization whose value is 0.001 in this paper. r_{j1} and r_{j2} ($r_{j1} \in [\delta, 1]$, $r_{j2} \in [0, 1]$, j = 1, 2, ..., N, N is the total number of elements on micro scale) are micro design variables,

Jiao Jia et al.
Two-scale topology optimization of macrostructure and porous microstructure composed of multiphase materials with distinct
Poisson's ratios

where r_{j1} characterizing the given micro element is solid material ($r_{j1} = 1$) or void ($r_{j1} = \delta$), and r_{j2} representing the existence of PPR ($r_{j2} = 1$) or NPR ($r_{j2} = 0$) base material. Adopting the structural compliance as the objective, two kinds of concurrent optimization problems are discussed to reveal the Poisson's ratio effect. In Problem A, the independent volume fraction constraints are imposed on macrostructure and microstructure; in Problem B, besides the coupled volume relationship between the macrostructure and microstructure, the thermal insulation constraint is conducted on micro-scale.
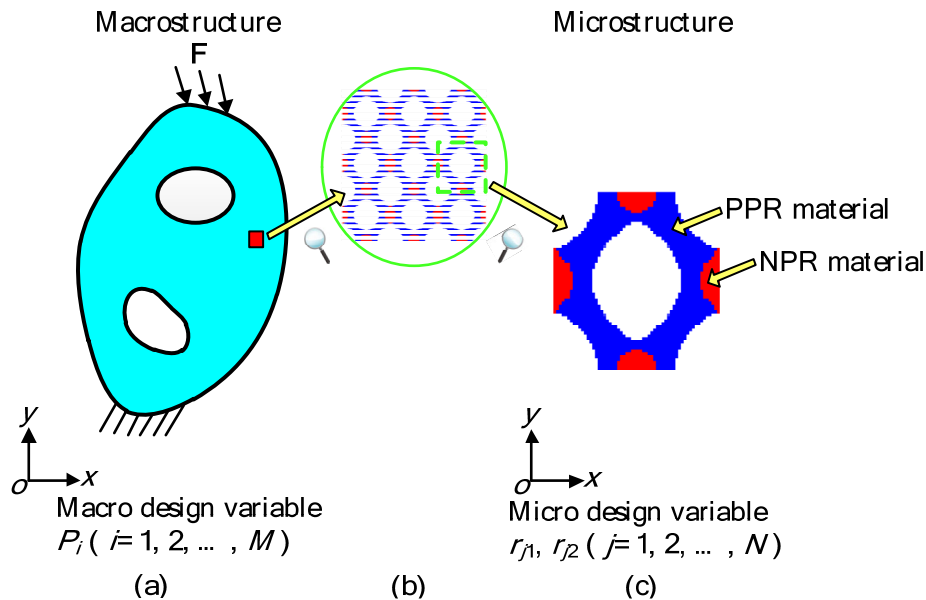

Figure 1: *A two scale system: (a) macrostructure; (b) periodic porous material; (c) porous microstructure.*

2.1 Problem A

In Problem A, the independent volume constraints are imposed on macrostructure and microstructure, the corresponding mathematical formula can be expressed as

$$
\begin{cases}
\text{Find}: \mathbf{X} = \{P_i, r_{j1}, r_{j2}\}\,(i = 1, 2, ..., M; j = 1, 2, ..., N) \\[2mm]
\text{Minimize:} \qquad C = \sum_{i=1}^{M} \mathbf{U}_i^T \mathbf{K}_i \mathbf{U}_i \\[2mm]
\text{Constraint I}: \qquad \mathbf{KU} = \mathbf{F} \\[2mm]
\text{Constraint II}: \qquad f^{\mathrm{mac}} = \sum_{i=1}^{M} P_i V_i / V^{\mathrm{mac}} \leq \overline{f^{\mathrm{mac}}} \\[2mm]
\text{Constraint III}: \qquad f^{\mathrm{mic,b}} = \sum_{j=1}^{N} r_{j1} V_j / V^{\mathrm{mic}} \leq \overline{f^{\mathrm{mic,b}}} \\[2mm]
\text{Constraint IV}: \qquad f^{\mathrm{mic,b1}} = \sum_{j=1}^{N} r_{j1} r_{j2} V_j / V^{\mathrm{mic}} \leq \overline{f^{\mathrm{mic,b1}}}
\end{cases}
\tag{1}
$$

where C denotes the macro structural compliance. $\mathbf{U}_i$ and $\mathbf{U}$ present the macro elemental and nodal displacement vectors, respectively. $\mathbf{K}_i$ and $\mathbf{K}$ are the macro elemental and global stiffness matrices, respectively. $\mathbf{F}$ is the external load vector applied on the macrostructure.

Constraint II defines the dosages of porous materials on macro-scale. V_i and V^{mac} respectively characterize the ith elemental volume and the volume of the macro design domain. f^{mac} denotes the prescribed volume fraction on macro-scale.

Jiao Jia et al.
Two-scale topology optimization of macrostructure and porous microstructure composed of multiphase materials with distinct
Poisson's ratios

Constraint III and IV respectively set the upper bounds on total base materials and PPR base material in microstructure. V_j and V^{mic} represent the $j\text{th}$ elemental volume and the volume of the micro design domain. $f^{\text{mic,b}}$ and $f^{\text{mic,b1}}$ are the prescribed volume fractions of base materials and PPR base material on micro-scale.

As known in Eq. (1), the volume fractions of the macrostructure and microstructure are respectively defined and there is no coupling relationship between the macro and micro design variables. That is to say the porous requirement on micro-scale is mandatory.

2.2 Problem B

In Problem B, the total dosages of the base materials and micro thermal insulation capability are simultaneously defined. The concurrent optimization model can be correspondingly expressed as

$$
\begin{cases}
\text{Find} : \mathbf{X} = \{P_i, r_{j1}, r_{j2}\}(i = 1,2,...,M; j = 1,2,...,N) \\[2mm]
\text{Minimize:} \quad C = \sum_{i=1}^{M} \mathbf{U}_i^T \mathbf{K}_i \mathbf{U}_i \\[2mm]
\text{Constraint I} : \mathbf{KU} = \mathbf{F} \\[2mm]
\text{Constraint II} : f^{\text{b}} = \dfrac{\sum_{i=1}^{M} P_i V_i}{V^{\text{mac}}} \dfrac{\sum_{j=1}^{N} r_{j1} V_j}{V^{\text{mic}}} \leq \overline{f^{\text{b}}} \\[4mm]
\text{Constraint III} : f^{\text{b1}} = \dfrac{\sum_{i=1}^{M} P_i V_i}{V^{\text{mac}}} \dfrac{\sum_{j=1}^{N} r_{j1} r_{j2} V_j}{V^{\text{mic}}} \leq \overline{f^{\text{b1}}} \\[4mm]
\text{Constraint IV} : \dfrac{1}{2} \sum_{s=1}^{2} \kappa_{ss}^{\text{H}} \leq \kappa_{\text{lim}}
\end{cases}
\tag{2}
$$

In Eq. (2), Constraint II and III respectively set the dosages of the base materials and PPR base material in macro and micro design domains. That is to say the macro and micro design variables have strong coupling relationship in volume fraction constraints.

Constraint IV describes the thermal insulation capability related to the microstructure. As to orthotropic material, the thermal insulation capability can be appraised according to the average of the diagonal elements in the effective thermal conductivity matrix [de Kruijf et al. 2007]. κ_{ss}^{H} is the sth diagonal element in the effective thermal conductivity matrix. κ_{lim} is the upper bound of the thermal conductivity. Actually, the thermal insulation constraint can also be understood as a porous requirement like volume fraction constraint, which not only restricts the dosages of the base materials on micro-scale but also plays a role of connecting the base materials.

2.3 Material interpolation scheme

2.3.1. Material interpolation scheme for structural analysis

Using SIMP scheme, the Young's modulus and Poisson's ratio in micro element j can be written as

$$E_j = r_{j1}^{\alpha}(r_{j2}^{\alpha} E^{(1)} + (1 - r_{j2}^{\alpha}) E^{(2)}) \tag{3a}$$

$$v_j = r_{j2}^{\beta} v^{(1)} + (1 - r_{j2}^{\beta}) v^{(2)} \tag{3b}$$

in which E and v respectively denote the Young's modulus and Poisson's ratio. Superscript numbers 1 and 2 characterize the PPR and NPR base materials, respectively. The penalization factors have the values of $\alpha = 4$ and $\beta = 1$ for better convergence and clearer topologies [Long et al. 2016].

For succinct programming, the Young's modulus and Poisson's ratio are substituted by the Lamé's parameters. As to 2D plane stress problem, the Lamé's parameters can be expressed as

Jiao Jia et al.
Two-scale topology optimization of macrostructure and porous microstructure composed of multiphase materials with distinct
Poisson's ratios

$$\lambda_{j} = E_{j}v_{j} / (1-v_{j}^{2}) \tag{4a}$$

$$\mu_{j} = E_{j} / (2(1+v_{j})) \tag{4b}$$

In 3D problem, the first Lamé's parameter needs to be modified as $\lambda_{i} = E_{i}v_{i} / (1+v_{i}) / (1-2v_{i})$, while the second Lame's parameter μ_{j} is kept the same with Eq. (4b).

With the help of Eq. (4), the elasticity matrix in microstructure can be split into

$$\mathbf{D}^{\mathrm{MI}} = \lambda_{j}\mathbf{D}_{\lambda} + \mu_{j}\mathbf{D}_{\mu} \tag{5}$$

where $\mathbf{D}_{\lambda}$ and $\mathbf{D}_{\mu}$ are the constant matrices with the expressions of $\mathbf{D}_{\lambda} = \begin{bmatrix} 1 & 1 & 0 \\ 1 & 1 & 0 \\ 0 & 0 & 0 \end{bmatrix}$, $\mathbf{D}_{\mu} = \begin{bmatrix} 2 & 0 & 0 \\ 0 & 2 & 0 \\ 0 & 0 & 1 \end{bmatrix}$ in 2D plane

stress problem, and $\mathbf{D}_{\lambda} = \begin{bmatrix} 1 & 1 & 1 & 0 & 0 & 0 \\ 1 & 1 & 1 & 0 & 0 & 0 \\ 1 & 1 & 1 & 0 & 0 & 0 \\ 0 & 0 & 0 & 0 & 0 & 0 \\ 0 & 0 & 0 & 0 & 0 & 0 \\ 0 & 0 & 0 & 0 & 0 & 0 \end{bmatrix}$, $\mathbf{D}_{\mu} = \begin{bmatrix} 2 & 0 & 0 & 0 & 0 & 0 \\ 0 & 2 & 0 & 0 & 0 & 0 \\ 0 & 0 & 2 & 0 & 0 & 0 \\ 0 & 0 & 0 & 1 & 0 & 0 \\ 0 & 0 & 0 & 0 & 1 & 0 \\ 0 & 0 & 0 & 0 & 0 & 1 \end{bmatrix}$ in 3D problem.

Effective elasticity matrix $\mathbf{D}^{\mathrm{H}}$ can be calculated by the numerical homogenization theory with the format of Lamé's parameters[Andreassen and Andreasen 2014, Hassani and Hinton 1998]

$$\mathbf{D}^{\mathrm{H}} = \frac{1}{|V|}\int_{V}(\lambda_{j}\mathbf{D}_{\lambda} + \mu_{j}\mathbf{D}_{\mu})(\mathbf{I} - \mathbf{bu})\mathrm{d}V \tag{6}$$

where $|V|$ is the volume of unit cell; $\mathbf{I}$ is the identity matrix; $\mathbf{b}$ is the micro strain-displacement matrix; the micro displacement field $\mathbf{u}$ can be acquired through the FE analysis with applying the periodic boundary conditions within the unit cell

$$\left(\int_{V}\mathbf{b}^{\mathrm{T}}\mathbf{D}^{\mathrm{MI}}\mathbf{b}\mathrm{d}V\right)\mathbf{u} = \int_{V}\mathbf{b}^{\mathrm{T}}\mathbf{D}^{\mathrm{MI}}\mathrm{d}V \tag{7}$$

The right hand side in Eq.(7) defines the external forces corresponding to the uniform strain fields, e.g., two normal unit strains in x and y directions and one shear unit strain for 2D cases, and three normal unit strains in x, y and z directions and three shear unit strains for 3D cases.

The macro elasticity matrix can be determined by the following interpolation

$$\mathbf{D}_{i}^{\mathrm{MA}} = P_{i}^{p}\mathbf{D}^{\mathrm{H}} \tag{8}$$

where the penalization factor p retains the typical value of 3.

From the above analysis, effective elasticity matrix $\mathbf{D}^{\mathrm{H}}$ plays a connection role between macrostructure and microstructure.

On macro-scale, FE analysis is again performed to obtain the displacement vector. The macro global stiffness matrix $\mathbf{K}$ can be assembled by the elemental stiffness matrix $\mathbf{K}_{i}$

$$\mathbf{K} = \sum_{i=1}^{M}\mathbf{K}_{i} = \sum_{i}^{M}\int_{V_{i}}\mathbf{B}^{\mathrm{T}}\mathbf{D}_{i}^{\mathrm{MA}}\mathbf{B}dV_{i} \tag{9}$$

where $\mathbf{B}$ denotes the macro strain-displacement matrix.

Jiao Jia et al.
Two-scale topology optimization of macrostructure and porous microstructure composed of multiphase materials with distinct
Poisson's ratios

2.3.2 Material interpolation scheme for thermal insulation constraint

When considering the Problem B, the effective thermal conductivity of the porous microstructure is needed. Similarly, the elemental thermal conductivity can be interpolated with the SIMP scheme

$$\kappa_j = r_{j1}^{\gamma}(r_{j2}^{\gamma}\kappa^{(1)} + (1 - r_{j2}^{\gamma})\kappa^{(2)}) \tag{10}$$

where $\kappa^{(1)}$ and $\kappa^{(2)}$ are respectively used to represent the thermal conductivity of PPR and NPR materials. It is supposed that $\kappa^{(1)} > \kappa^{(2)}$. γ is the penalization factor with the value of 4 [Jia et al. 2016].

Furthermore, the micro thermal conductivity matrix can be obtained as

$$\kappa^{\mathrm{MI}} = \kappa_j \mathbf{k}_0 \tag{11}$$

where $\mathbf{k}_0$ is the basic thermal conductivity matrix when thermal conductivity is 1.

Similarly, the effective thermal conductivity matrix $\mathbf{k}^{\mathrm{H}}$ can also be evaluated through the numerical homogenization method

$$\mathbf{k}^{\mathrm{H}} = \frac{1}{|V|}\int_V \mathbf{k}^{\mathrm{MI}}(\mathbf{I}_s - \boldsymbol{\chi})\mathrm{d}V \tag{12}$$

where $\mathbf{I}_s$ represents the identity matrix in the process of thermal conductivity homogenization; $\boldsymbol{\chi}$ denotes the induced temperature gradient field which can be computed from the uniform gradient temperature fields.

More details in implementation of homogenized elasticity and thermal conductivity matrices can be referred to literature [Andreassen and Andreasen 2014].

3 SENSITIVITY ANALYSES FOR MACROSTRUCTURES AND MICROSTRUCTURES

Basing on the adjoint variable method [Haug, Choi, and Komkov 1986], the derivatives of the objective to the design variables can be calculated as

$$\frac{\partial C}{\partial P_i} = -\mathbf{U}^{\mathrm{T}}\frac{\partial \mathbf{K}}{\partial P_i}\mathbf{U} = -pP_i^{p-1}\mathbf{U}_i^{\mathrm{T}}\int_{V_i}\mathbf{B}^{\mathrm{T}}\mathbf{D}^{\mathrm{H}}\mathbf{B}dV_i\mathbf{U}_i \tag{13}$$

$$\frac{\partial C}{\partial r_{jk}} = -\mathbf{U}^{\mathrm{T}}\frac{\partial \mathbf{K}}{\partial r_{jk}}\mathbf{U} = -\sum_{i=1}^{M}\mathbf{U}_i^{\mathrm{T}}\frac{\partial \mathbf{K}_i}{\partial r_{jk}}\mathbf{U}_i = -\sum_{i=1}^{M}P_i^p\mathbf{U}_i^{\mathrm{T}}\int_{V_i}\mathbf{B}^{\mathrm{T}}\frac{\partial \mathbf{D}^{\mathrm{H}}}{\partial r_{jk}}\mathbf{B}dV_i\mathbf{U}_i \tag{14}$$

According to the mapping method [Liu et al. 2002], the expression of $\partial\mathbf{D}^{\mathrm{H}}\big/\partial r_{jk}$ (k=1, 2) in Eq. (14) can be written as

$$\frac{\partial \mathbf{D}^{\mathrm{H}}}{\partial r_{jk}} = \frac{1}{|V|}\int_V(\mathbf{I} - \mathbf{bu})^{\mathrm{T}}\frac{\partial \mathbf{D}^{\mathrm{MI}}}{\partial r_{jk}}(\mathbf{I} - \mathbf{bu})dV \tag{15}$$

With the aid of Eq. (5), the above equation can be further given as

$$\frac{\partial \mathbf{D}^{\mathrm{H}}}{\partial r_{jk}} = \frac{1}{|V|}\int_V(\mathbf{I} - \mathbf{bu})^{\mathrm{T}}\frac{\partial \lambda_j}{\partial r_{jk}}\mathbf{D}_{\lambda}(\mathbf{I} - \mathbf{bu})dV + \frac{1}{|V|}\int_V(\mathbf{I} - \mathbf{bu})^{\mathrm{T}}\frac{\partial \mu_j}{\partial r_{jk}}\mathbf{D}_{\mu}(\mathbf{I} - \mathbf{bu})dV \tag{16}$$

in which $\partial\lambda_j\big/\partial r_{jk}$ and $\partial\mu_j\big/\partial r_{jk}$ can be attained by the chain rule

$$\partial\lambda_j\big/\partial r_{jk} = \frac{\partial \lambda_j}{\partial E_j}\frac{\partial E_j}{\partial r_{jk}} + \frac{\partial \lambda_j}{\partial v_j}\frac{\partial v_j}{\partial r_{jk}} \tag{17a}$$

$$\partial \mu_j \big/ \partial r_{jk} = \frac{\partial \mu_j}{\partial E_j}\frac{\partial E_j}{\partial r_{jk}} + \frac{\partial \mu_j}{\partial v_j}\frac{\partial v_j}{\partial r_{jk}} \tag{17b}$$

where $\partial \lambda_j \big/ \partial E_j$ has distinct expressions in 2D plane stress and 3D problems, as

$$\partial \lambda_j \big/ \partial E_j = v_j \big/ (1 - v_j^2) \text{ (2D plane stress)} \tag{18a}$$

$$\partial \lambda_j \big/ \partial E_j = v_j \big/ (1 + v_j) \big/ (1 - 2v_j) \text{ (3D)} \tag{18b}$$

Furthermore, the expression of $\partial E_j \big/ \partial r_{jk}$ in Eq. (17) can be calculated as

$$\partial E_j \big/ \partial r_{j1} = p r_{j1}^{(\alpha-1)}(E^{(1)} r_{j2}^{\alpha} + E^{(2)}(1 - r_{j2}^{\alpha})) \tag{19a}$$

$$\partial E_j \big/ \partial r_{j2} = p r_{j1}^{\alpha} r_{j2}^{(\alpha-1)}(E^{(1)} - E^{(2)}) \tag{19b}$$

Similar as $\partial \lambda_j \big/ \partial E_j$, $\partial \lambda_j \big/ \partial v_j$ also possesses distinct expressions in 2D plane stress and 3D problems, as

$$\partial \lambda_j \big/ \partial v_j = E_j(1 + v_j^2) \big/ (1 - v_j^2)^2 \text{ (2D plane stress)} \tag{20a}$$

$$\partial \lambda_j \big/ \partial v_j = E_j(1 + 2v_j^2) \big/ (1 + v_j)^2 \big/ (1 - 2v_j)^2 \text{ (3D)} \tag{20b}$$

For r_{j1} is independent of v_j, it only has

$$\partial v_j \big/ \partial r_{j2} = q r_{j2}^{(\beta-1)}(v^{(1)} - v^{(2)}) \tag{21}$$

In Eq. (17b), $\partial \mu_j \big/ \partial E_j$ and $\partial \mu_j \big/ \partial v_j$ can be respectively derived from Eq. (4b)

$$\partial \mu_j \big/ \partial E_j = 1 \big/ (2(1 + v_j)) \tag{22}$$

$$\partial \mu_j \big/ \partial v_j = -E_j \big/ (1 + v_j)^2 \big/ 2 \tag{23}$$

Eqs. (14)-(16) clearly indicate that the sensitivity expressions for micro design variables are split into two parts with the help of Lamé's parameters, which simplifies the deduction process and programming.

In Problem A, the derivatives of volume fractions with the design variables on macro and micro scales can be respectively given as

$$\frac{\partial f^{\mathrm{mac}}}{\partial P_i} = V_i \big/ V^{\mathrm{mac}} \;, \; \frac{\partial f^{\mathrm{mac}}}{\partial r_{j1}} = 0 \;, \; \frac{\partial f^{\mathrm{mac}}}{\partial r_{j2}} = 0 \tag{24}$$

$$\frac{\partial f^{\mathrm{mic,b}}}{\partial P_i} = 0 \;, \; \frac{\partial f^{\mathrm{mic,b}}}{\partial r_{j1}} = \frac{V_j}{V^{\mathrm{mic}}} \;, \; \frac{\partial f^{\mathrm{mic,b}}}{\partial r_{j2}} = 0 \tag{25}$$

$$\frac{\partial f^{\mathrm{mic,b1}}}{\partial P_i} = 0 \;, \; \frac{\partial f^{\mathrm{mic,b1}}}{\partial r_{j1}} = \frac{r_{j2}V_j}{V^{\mathrm{mic}}} \;, \; \frac{\partial f^{\mathrm{mic,b1}}}{\partial r_{j2}} = \frac{r_{j1}V_j}{V^{\mathrm{mic}}} \tag{26}$$

When considering Problem B, the derivatives of volume fractions with respect to the design variables can be followed as

$$\frac{\partial f^{\mathrm{b}}}{\partial P_i} = \frac{V_i}{V^{\mathrm{mac}}} \frac{\sum_{j=1}^{N} r_{j1} V_j}{V^{\mathrm{mic}}}, \quad \frac{\partial f^{\mathrm{b}}}{\partial r_{j1}} = \frac{\sum_{i=1}^{M} P_i V_i}{V^{\mathrm{mac}}} \frac{V_j}{V^{\mathrm{mic}}}, \quad \frac{\partial f^{\mathrm{b}}}{\partial r_{j2}} = 0 \tag{27}$$

$$\frac{\partial f^{\mathrm{b1}}}{\partial P_i} = \frac{V_i}{V^{\mathrm{mac}}} \frac{\sum_{j=1}^{N} r_{j1} r_{j2} V_j}{V^{\mathrm{mic}}}, \quad \frac{\partial f^{\mathrm{b1}}}{\partial r_{j1}} = \frac{\sum_{i=1}^{M} P_i V_i}{V^{\mathrm{mac}}} \frac{r_{j2} V_j}{V^{\mathrm{mic}}}, \quad \frac{\partial f^{\mathrm{b1}}}{\partial r_{j2}} = \frac{\sum_{i=1}^{M} P_i V_i}{V^{\mathrm{mac}}} \frac{r_{j1} V_j}{V^{\mathrm{mic}}} \tag{28}$$

Moreover, the derivatives of κ_{ss}^{H} with respect to design variables are needed. Due to κ_{ss}^{H} is independent of the macro design variable P_i, $\partial \kappa_{ss}^{\mathrm{H}} / \partial P_i = 0$. With the help of Eqs. (10) and (11), the derivatives of κ_{ss}^{H} with respect to r_{jk} can be written as

$$\frac{\partial \kappa_{ss}^{\mathrm{H}}}{\partial r_{j1}} = \frac{\gamma r_{j1}^{(\gamma-1)} (\kappa^{(1)} \gamma_{j2}^{\gamma} + \kappa^{(2)} (1 - r_{j2}^{\gamma}))}{|V|} \int_{V_j} (\mathbf{I}^s - \boldsymbol{\chi}_j^s)^{\mathrm{T}} \mathbf{k}_0 (\mathbf{I}^s - \boldsymbol{\chi}_j^s) dV_j \tag{29a}$$

$$\frac{\partial \kappa_{ss}^{\mathrm{H}}}{\partial r_{j2}} = \frac{\gamma r_{j1}^{\gamma} \gamma_{j2}^{(\gamma-1)} (\kappa^{(1)} - \kappa^{(2)})}{|V|} \int_{V_j} (\mathbf{I}^s - \boldsymbol{\chi}_j^s)^{\mathrm{T}} \mathbf{k}_0 (\mathbf{I}^s - \boldsymbol{\chi}_j^s) dV_j \tag{29b}$$

4 NUMERICAL IMPLEMENTATION AND PROCEDURE

In this article, the heuristic sensitivity filtering technique [Sigmund 1997] is adopted to eliminate checkerboard patterns and mesh dependence.

For design variables P_i and r_{j1} respectively representing the material or void on macro and micro scales, the classical mesh-independency filter with weighting the element density is employed. Taken P_i as an example

$$\frac{\partial C}{\partial P_i} = \frac{1}{P_i \sum_{e \in R_i} H_{ie}} \sum_{e \in R_i} H_{ie} P_e \frac{\partial C}{\partial P_e} \tag{30}$$

where R_i is the set of elements e for which the center-to-center distance $\Delta(i,e)$ to element i is smaller than the filter radius r_{min} and H_{ie} is a weight factor determined by

$$H_{ie} = \max \left(0, r_{\mathrm{min}} - \Delta(i,e)\right) \tag{31}$$

For r_{j2} is no longer a simple density variable and the suggested filter should be expressed as [Sigmund 2001]

$$\frac{\partial C}{\partial r_{j2}} = \frac{1}{\sum_{e \in N_j} H_{je}} \sum_{e \in N_j} H_{je} \frac{\partial C}{\partial r_{e2}} \tag{32}$$

Averaging of the sensitivities will produce blurry boundaries in final topologies. For eliminating the intermediate density, the filtering programs are terminated after $\| \mathbf{X}^{(l+1)} - \mathbf{X}^{(l)} \| / \| \mathbf{X}^{(l+1)} \| \leq 0.5\%$, where $\mathbf{X} = \mathbf{P} \cup \mathbf{r}$ ($\mathbf{P} = \{P_i, i = 1, 2, ..., M\}$; $\mathbf{r} = \{r_{jk}, j = 1, 2, ..., N; k = 1, 2\}$) and l stands for the current iteration. Then the optimization procedure will continue without filtering until $\| \mathbf{X}(l+1) - \mathbf{X}(l) \| / \| \mathbf{X}(l+1) \| \leq 0.1\%$.

In Problem A, the optimality criteria (OC) method is employed in macro-scale optimization, and the method of moving asymptotes (MMA) [Svanberg 1987] is utilized as the optimizer in micro-scale. In Problem B, only MMA is adopted as an optimization solver.

Jiao Jia et al.
Two-scale topology optimization of macrostructure and porous microstructure composed of multiphase materials with distinct
Poisson's ratios

Key steps for the concurrent design of macrostructure and microstructure with PPR and NPR base materials are given in Fig. 2.

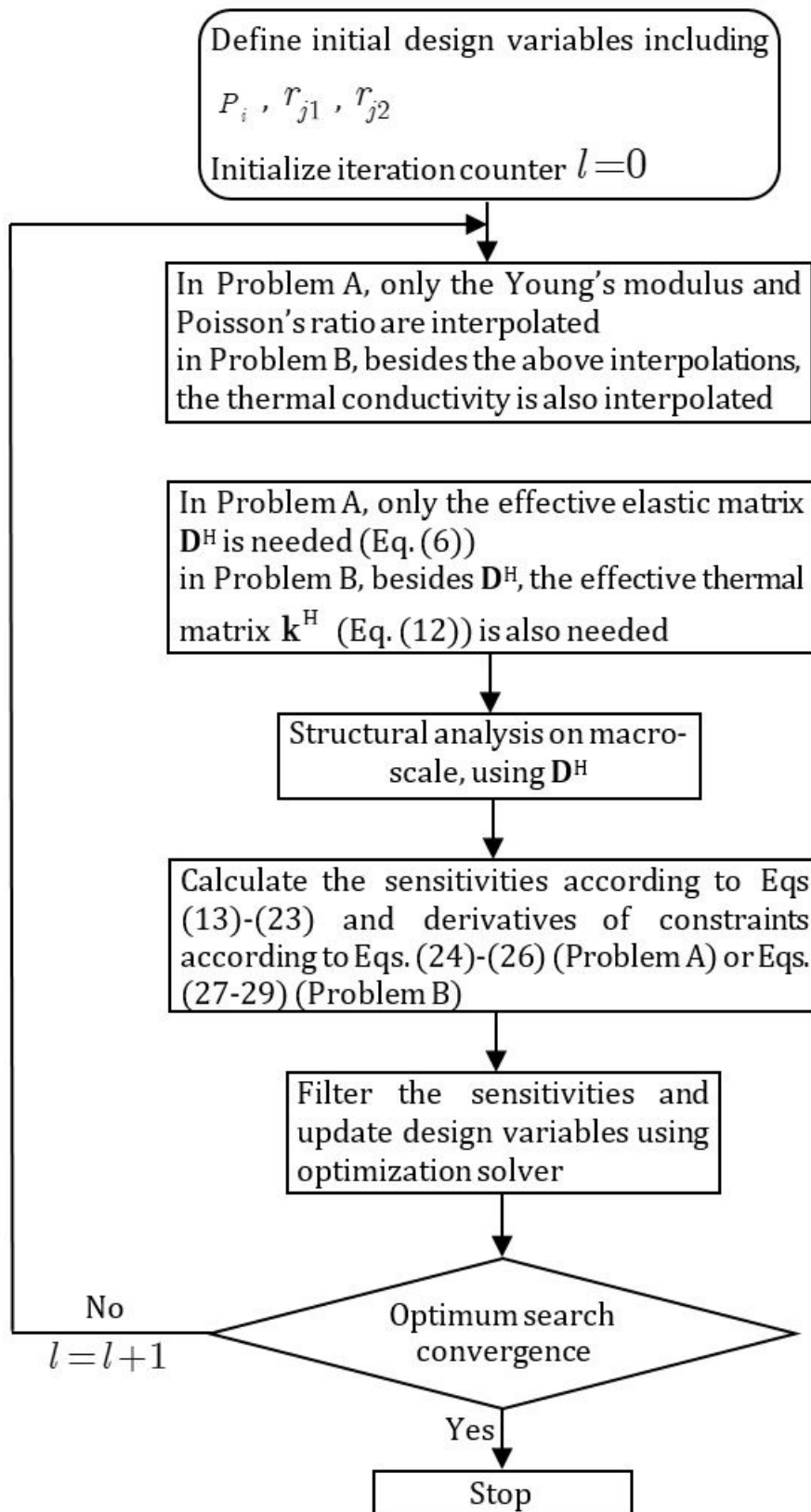Define initial design variables including

P_i , r_{j1} , r_{j2}

Initialize iteration counter $l = 0$

↓

In Problem A, only the Young's modulus and Poisson's ratio are interpolated
in Problem B, besides the above interpolations, the thermal conductivity is also interpolated

↓

In Problem A, only the effective elastic matrix $\mathbf{D}^H$ is needed (Eq. (6))
in Problem B, besides $\mathbf{D}^H$, the effective thermal matrix $\mathbf{k}^H$ (Eq. (12)) is also needed

↓

Structural analysis on macro-scale, using $\mathbf{D}^H$

↓

Calculate the sensitivities according to Eqs (13)-(23) and derivatives of constraints according to Eqs. (24)-(26) (Problem A) or Eqs. (27-29) (Problem B)

↓

Filter the sensitivities and update design variables using optimization solver

↓

No
$l = l + 1$

Optimum search convergence

Yes

Stop

Figure 2: *Flowchart of concurrent design with PPR and NPR base materials*

Jiao Jia et al.
Two-scale topology optimization of macrostructure and porous microstructure composed of multiphase materials with distinct
Poisson's ratios

5 ILLUSTRATIVE EXAMPLES AND DISCUSSIONS

In this section, we present several 2D and 3D numerical examples for concurrent design with considering the Poisson's ratio effect in concurrent structure. Where two 2D examples and one 3D example are discussed in Problem A corresponding to two 2D examples for Problem B. For easier discussions, the structural sizes, material properties and external loads are all dimensionless. In 2D examples, the microstructure is discretized into 60×60 4-node quadrilateral elements, and 26×26×26 8-node solid elements in 3D example. The macro element edge is 1. As shown in Fig. 3, two types of non-uniform initial distributions on micro-scale are adopted in this study. Where initial design I and II are applied in 2D problem and initial design III is used in 3D problem. The density in initial design I and III is proportional to the distance from the element center to the center of the microstructure. The initial design II originates from the literature [Zhou et al. 2012]. In Problem A, r_{j1} starts from the initial design I (2D) or III (3D) and r_{j2} starts from the uniform density distribution. In Problem B, r_{j1} starts from the initial design II and r_{j2} starts from the initial design I.
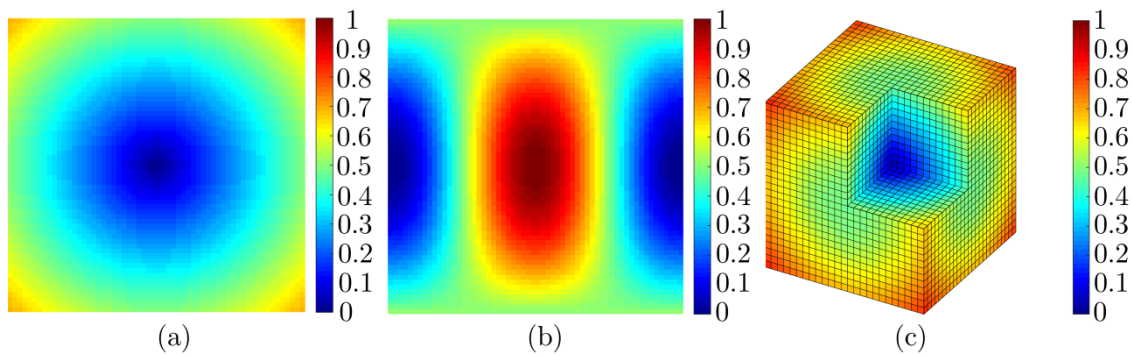
Figure 3: *Density distribution in micro design domain: (a) initial design I; (b) initial design II;(c) initial design III.*

For ensuring close Young's moduli to each other, the base materials are assumed to be polymers and designed in the form of porous microstructures. In all the numerical examples, the Young's modulus of the base material 1 is defined as $E^{(1)} = 2.1$. The Poisson's ratio of the base material 1 is supposed to be $v^{(1)} = 0.4$ in the first four examples and $v^{(1)} = 0.35$ in the last example. For easy identification, PPR and NPR base materials in microstructures are respectively plotted in blue and red. Although the strategy with overcoming intermediate densities is adopted, a handful of intermediate densities still exist in the final topologies. For more meaningful comparisons, all the optimized results are executed with the 0-1 post processing [Sigmund and Maute 2013].

5.1 Problem A

In Problem A, the Young's modulus of the base material 2 is set as $E^{(2)} = 1.8$.

Example I

The Poisson's ratio effect in concurrent design is illustrated in this example. As shown in Fig. 4, the dimensions of the macro design domain are: length L=50, height H=100. The left edge is fully constrained and subjected to a vertical downward load, F=10, at the center of the right edge. $v^{(2)}$ is allowed to vary from -0.4 to -0.9. The target macro and micro volume fractions are predefined as f^{mac}=50%, $f^{\text{mic,b}}$=50% and $f^{\text{mic,b1}}$=40%.

Fig.5 plots the evolution histories of the macro and micro densities with $v^{(2)}$=-0.4. This process clearly illustrates that the macrostructure and microstructure rapidly converge to stable topologies within fewer iteration steps. Fig. 6 provides the resulting compliance under various $v^{(2)}$. Several quintessential topologies with $v^{(2)}$ = -0.4, -0.6, -0.7 and -0.9 are inserted above the resulting compliance curve. For the sake of comparison, the optimized results with exclusive NPR base material are also presented in Fig. 6. At the mean time, the optimized macrostructure and microstructure from exclusive PPR base material are shown in Fig. 7. The corresponding compliance is C =3946.37. From Figs. 6 and 7, it is known that the macrostructure composed of PPR and NPR base materials can provide a lower system compliance than that from the exclusive PPR or NPR base material. Moreover, the resulting compliance presents a tendency to decline with the decrement of $v^{(2)}$ (from -0.4 to -0.9) and the minimum

compliance occurs when the difference of $v^{(1)}$ and $v^{(2)}$ reaching the maximum ($v^{(1)}$ =0.4 and $v^{(2)}$ =-0.9 in this example).
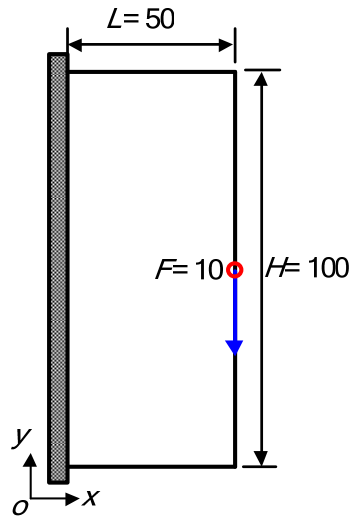

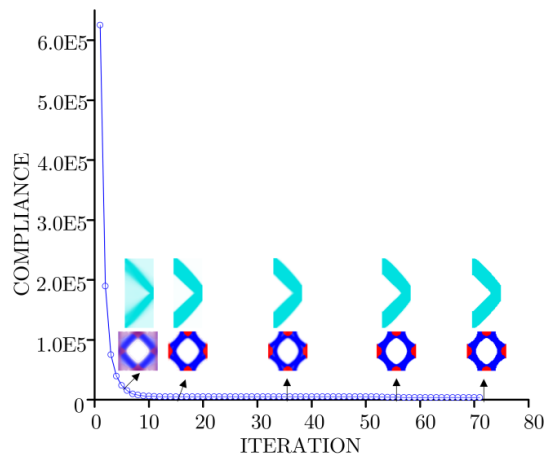**Figure 4:** A 2D cantilever beam for example I with length L=50, height H=100.

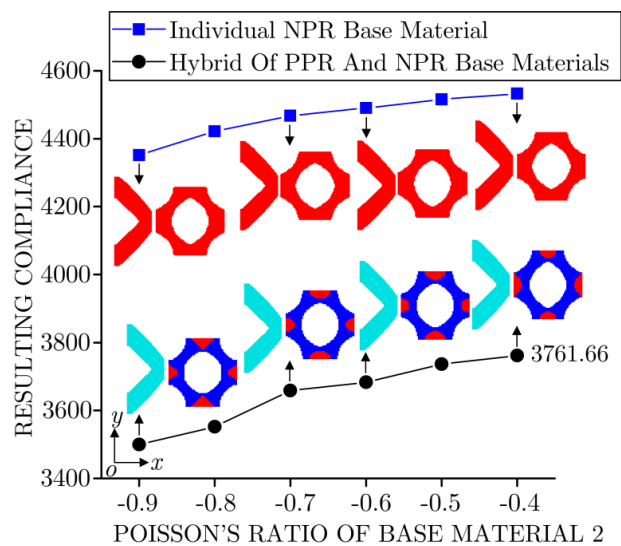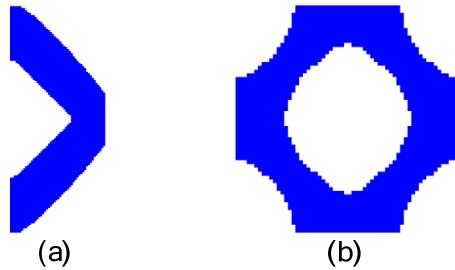**Figure 5:** Evolution histories of macro and micro densities.

Figure 6: The influence of NPR on the resulting compliance

| (a) | (b) |

Figure 7: *The optimized results composed of exclusive PPR base material: (a) macrostructure; (b) microstructure.*

Example II

In this example, a long beam is optimized to investigate the influence of volume fractions on the final solution. As shown in Fig. 8, the overall sizes of the macro design domain are: length L=300, height H=50. A concentrated downward load is applied vertically at the center of the top edge with the bottom corners fully fixed. Considering the symmetry, only right half of the structure is used for optimization and result discussion. The load magnitude on the half beam is assumed to be F=5. The permitted variation ranges of $v^{(2)}$ are from -0.4 to -0.7. The volume fraction of PPR base material on micro-scale $f^{\text{mic,bl}}$ changes from 10% to 40% while f^{mac} and $f^{\text{mic,b}}$ are both fixed at 50%.
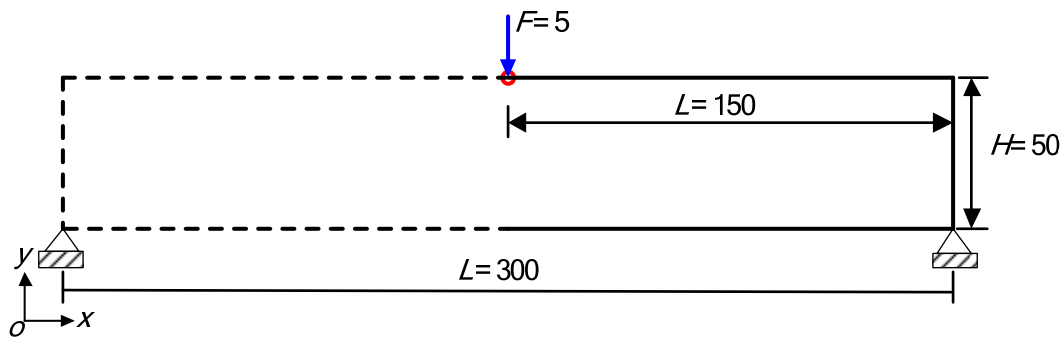
Figure 8: *A 2D long beam for example III with length L=300, height H=50.*

Fig. 9 provides the variation trend of resulting compliance under various $f^{\text{mic,bl}}$. Moreover, the resulting topologies with $f^{\text{mic,bl}}$=10%, 25% and 40% when $v^{(2)}$=-0.4, -0.7 are inserted at intervals in Fig. 9. To aid comparisons, the objective values and topologies with exclusive PPR and NPR base materials (only $v^{(2)}$=-0.4) are included as well in Fig. 9. All the detailed data are summarized in Table 1. Unlike the Poisson's ratio, in Fig. 9, the resulting compliance does not present a monotonic relationship with increasing of $f^{\text{mic,bl}}$, i.e., there is an optimal $f^{\text{mic,bl}}$ corresponding to the minimum compliance with a fixed $v^{(2)}$. In addition, from Fig. 9 and Table 1, it is observed that the optimal volume fraction $f^{\text{mic,bl}}$ varies with $v^{(2)}$. The detailed variations of $f^{\text{mic,bl}}$ are followed as: as to $v^{(2)}$=-0.4 and $v^{(2)}$=-0.5, the summit of the resulting compliance occurs when $f^{\text{mic,bl}}$ is approximately 40%, and as to $v^{(2)}$=-0.6 and $v^{(2)}$=-0.7, the minimum resulting compliance transfers to near $f^{\text{mic,bl}}$=35%. This is primarily due to the stiffness of NPR base material is improved when $v^{(2)}$ is constantly decreasing. Furthermore, the ranges of $f^{\text{mic,bl}}$ whose objective values can exceed the results of exclusive PPR and NPR base materials are gradually enlarged with decreasing of $v^{(2)}$, i.e., $f^{\text{mic,bl}}$ varies 35% to 40% when $v^{(2)}$=-0.4 and $v^{(2)}$=-0.5, $f^{\text{mic,bl}}$ varies from 25% to 40% when $v^{(2)}$=-0.6, and $f^{\text{mic,bl}}$ varies from 20% to 40% when $v^{(2)}$=-0.7. For clarity, the objective values corresponding to the above mentioned volume fractions are highlighted in Table 1.
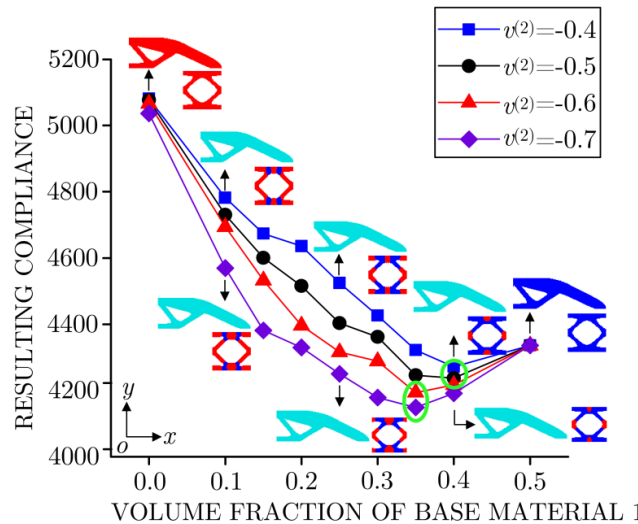
Figure 9: *The influence of the volume fraction of base material 1 on the resulting compliance.*

Table 1: *The resulting compliance under various $f^{\text{mic,b1}}$.*

$f^{\text{mic,b1}}$ (%)	Resulting compliance when $v^{(2)}$=-0.4	Resulting compliance when $v^{(2)}$=-0.5	Resulting compliance when $v^{(2)}$=-0.6	Resulting compliance when $v^{(2)}$=-0.7
0	5081.84	5076.73	5066.70	5036.28
10	4781.77	4730.34	4694.58	4569.17
15	4673.54	4600.76	4532.29	4381.39
20	4636.04	4515.19	4396.53	4329.66
25	4524.70	4403.61	4315.74	4249.85
30	4426.43	4361.56	4288.50	4178.48
35	4321.60	4246.08	4193.36	4148.40
40	4271.43	4237.43	4216.97	4191.12
50	4335.96	4335.96	4335.96	4335.96

Example III

A 3D cantilever beam is optimized in this example to demonstrate the adaptability of the proposed model in 3D concurrent design. Fig. 10 shows the admissible design domain in macrostructure with sizes of length L=48, height H=30, and width B=8. The left hand side surface is fully constrained and an evenly distributed load F=5 is applied at the middle of the right surface. The Poisson's ratio of the base material 2 is set as $v^{(2)}$=-0.7. The volume fraction constraints at two scales are set as f^{mac}=30%, $f^{\text{mic,b}}$=80%, and $f^{\text{mic,b1}}$=40%.

Table 2 lists the resulting two-scale topologies and effective elasticity matrix from hybrid of PPR and NPR base materials. At the mean time, the results of traditional structures made of exclusive PPR and NPR base materials with identical macro volume constraint f^{mac}=30% are provided as well in Table 2. According to the previous research [Niu, Yan, and Cheng 2009, Vicente et al. 2016, Yan, Cheng, and Liu 2008], the macrostructure composed of porous microstructure cannot provide higher stiffness than the traditional structure without porosity on microscale. However, from Table 2, a lower resulting compliance is observed in the concurrent design from porous microstructure. It is should be attributed to the Poisson's ratio effect.
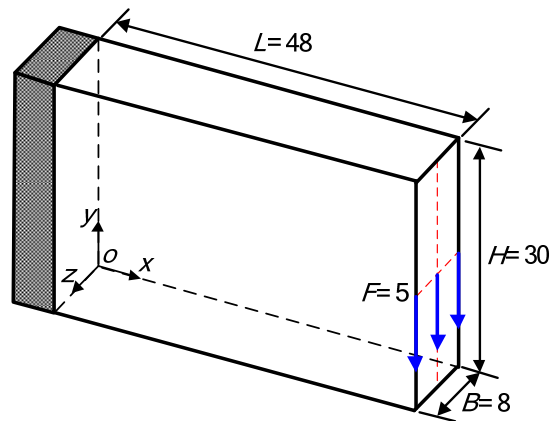
Figure 10: *A 3D cantilever for example III with length L=48, height H=30 and width B=8.*

Table 2: *The comparisons of concurrent structure and traditional structure.*

$f^{\text{mic,b}}$ (%)	$f^{\text{mic,b1}}$ (%)	Resulting compliance	Macro-structure	Micro-structure	Elasticity matrix
100	100	7021.37			
80	40	6125.68			$\begin{bmatrix} 2.5683 & -0.0935 & -0.1389 & 0.0000 & 0.0001 & 0.0000 \\ -0.0935 & 2.0672 & 0.4953 & -0.0000 & 0.0002 & 0.0000 \\ -0.1389 & 0.4953 & 1.1611 & -0.0000 & 0.0000 & 0.0000 \\ 0.0000 & -0.0000 & -0.0000 & 1.1608 & -0.0000 & 0.0000 \\ 0.0001 & 0.0002 & 0.0000 & -0.0000 & 0.6976 & -0.0000 \\ 0.0000 & 0.0000 & 0.0000 & 0.0000 & -0.0000 & 0.9563 \end{bmatrix}$
100	0	6982.06			

5.2 Problem B

In Problem B, Young's modulus of the base material 2 is assumed to be $E^{(2)} = 1.7$. The thermal conductivities of the base materials are kept to be $\kappa^{(1)} = 6$, $\kappa^{(2)} = 4$. The total dosages of the base materials are fixed at $f^{\text{b}} = 50\%$. $f^{\text{mic,b2}}$ is used to represent the volume fraction of the base material 2 in microstructure.

Example IV

The influences of NPR and volume fraction f^{b1} are investigated in this example. As shown in Fig. 11, the macro design domain has sizes of length $L=160$, height $H=100$ with the same boundary condition and external load as illustrated in example I. Poisson's ratio of the base material 2 is set to be $v^{(2)} = -0.3, -0.4$ and -0.6, respectively. f^{b1} is allowed to vary from 10% to 40%. The upper limit of the effective thermal conductivity is defined as $\kappa_{\text{lim}} = 2$.
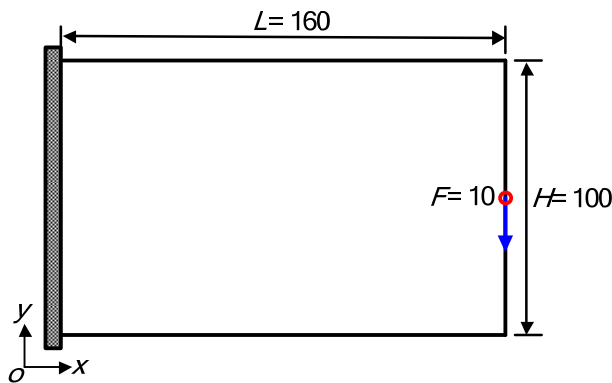
Figure 11: *A 2D cantilever beam for example IV with length L=160, height H=100.*

Fig. 12 supplies the resulting compliance under various f^{b1}. In addition, several typical topologies with f^{b1} =10%, 20%, 30% and 40% when $v^{(2)}$=-0.6 are inserted in Fig. 12. For comparison, the optimized results with exclusive base material 1 and 2 (only $v^{(2)}$=-0.6) are also given in Fig. 12. All the detailed data are summarized in Table 3. From Fig. 12, it is can be easily found that the macro and micro structures respectively exhibit the disparate topological configurations with increasing of f^{b1}. In order to manifest the stiffness enhancement is not caused by the variations of the macro and micro topological configurations, the optimized results with $v^{(2)}$=0.4 are also presented in Fig. 12. In Fig.12, it is noted that the resulting compliance from exclusive base material 2 is lower than the value of exclusive base material 1. Moreover, when $v^{(2)}$=0.4, the minimum resulting compliance from multiphase materials is found to be between the values of exclusive base material 1 and 2, i.e., the concurrent stiffness is not be enhanced by blending two PPR base materials. However, when $v^{(2)}$=-0.3, -0.4 and -0.6, the resulting stiffness can be enhanced at certain ranges of f^{b1}. The above analysis proves that the stiffness enhancement is caused by the hybrid of PPR and NPR base materials. Similar with the Problem A, in Problem B the resulting compliance also decreases monotonically with the decrement of $v^{(2)}$ (from -0.3 to -0.6). Moreover, with the reduction of $v^{(2)}$, the ranges of f^{b1} for enhanced stiffness are keeping expanding, i.e., f^{b1} is equal to 10% when $v^{(2)}$=-0.3, f^{b1} varies from 10% to 15% when $v^{(2)}$=-0.4 and f^{b1} varies from 10% to 20% when $v^{(2)}$=-0.6. For clarity, the objective values corresponding to the above mentioned volume fractions are highlighted in Table 3. However, unlike in Problem A, the optimal volume fraction does not change with the variation of NPR in Problem B. That is to say the resulting compliance increases monotonically with the increment of f^{b1}.
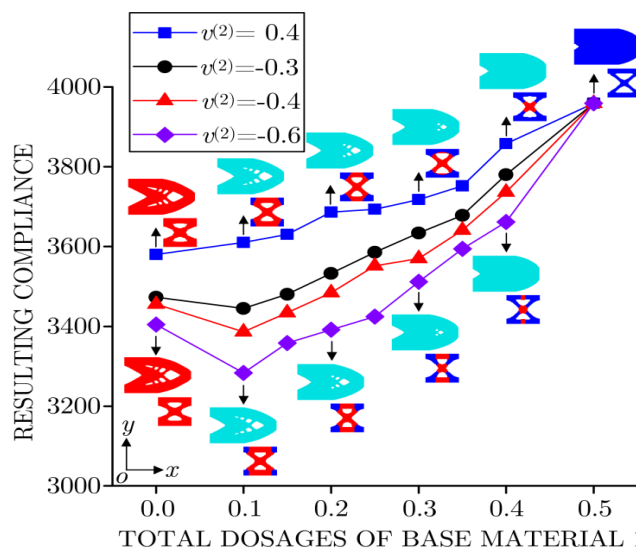

Figure 12: *The influences of NPR and volume fraction of base material 1 on the resulting compliance.*

Table 3: *The resulting compliance under various f^{b1} when $v^{(2)}$ =0.4, -0.3, -0.4 and -0.6.*
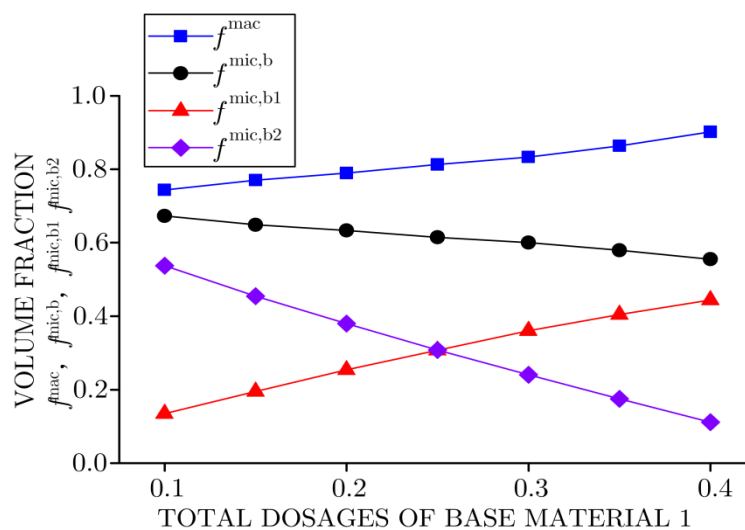
f^{b1} (%)	Resulting compliance when $v^{(2)}$ = 0.4	Resulting compliance when $v^{(2)}$ =-0.3	Resulting compliance when $v^{(2)}$ =-0.4	Resulting compliance when $v^{(2)}$ =-0.6
0	3580.15	3473.04	3455.35	3404.13
10	3610.49	3444.89	3386.12	3283.07
15	3630.29	3480.43	3434.12	3358.06
20	3686.04	3532.51	3483.96	3391.87
25	3693.22	3585.78	3551.08	3424.85
30	3717.45	3633.84	3570.02	3511.59
35	3752.09	3678.20	3641.47	3594.40
40	3857.64	3779.87	3736.58	3661.57
50	3959.25	3959.25	3959.25	3959.25

When $v^{(2)}$ =0.4, -0.6, the distributions of the base materials in microstructures seem different especially under larger f^{b1}, e.g., f^{b1} =30% and 40%. For better illustration, taken f^{b1} =40% as an example, the objective value is revaluated after exchanging the material parameters for each other, i.e., respectively take $v^{(2)}$ =0.4 and $v^{(2)}$ =-0.6 into the topologies of hybrid of PPR and NPR base materials and hybrid of two PPR base materials. The detailed data are listed in Table 4. The comparisons show that both the original optimized results have lower compliance values which illustrates that with the variation of $v^{(2)}$, the diverse distributions of base materials seem reasonable. This is mainly due to the stiffness of the base material 2 changes with the variation of $v^{(2)}$.

Taken $v^{(2)}$ =-0.3 as an example, the trends of f^{mac}, $f^{mic,b}$, $f^{mic,b1}$ and $f^{mic,b2}$ under various f^{b1} are shown in Fig. 13. In Fig. 13, it is observed that with f^{b1} varying from 10%-40%, f^{mac} and $f^{mic,b1}$ increase while $f^{mic,b}$ and $f^{mic,b2}$ decrease. According to the Constraints II and III in Eq. (2), fixed f^b and increased f^{b1} result in more PPR base materials distributing on micro-scale. At the mean time, due to the thermal insulation constraint having no change, less NPR base materials are required in microstructure. Consequently, even with $f^{mic,b1}$ continuously increasing, $f^{mic,b}$ still demonstrates a decline trend for degressive $f^{mic,b2}$. Finally, f^{mac} presents an uptrend because of fixed f^b and decreased $f^{mic,b}$.

Table 4: *Cross checks for $v^{(2)}$ =0.4 and $v^{(2)}$ =-0.6.*

$v^{(2)}$	Resulting compliance	Compliance of cross check
0.4	3857.64	3895.75
-0.6	3661.57	3737.16

Figure 13: *The influences of f^{b1} on f^{mac}, $f^{mic,b}$, $f^{mic,b1}$ and $f^{mic,b2}$.*

Jiao Jia et al.
Two-scale topology optimization of macrostructure and porous microstructure composed of multiphase materials with distinct
Poisson's ratios

Example V

This example is the extension of example IV, with an attempt to reveal the influence of thermal insulation constraint on the final results. The design domain, boundary condition and external load are kept the same with the example IV. The Poisson's ratio of the base material 2 is set as $v^{(2)}$ =-0.5, and the total dosages of the base material 1 is fixed at f^{b1} =20%. The thermal insulation constraint varies from 2 to 3.5.

Under various $\kappa_{\lim}$, Fig. 14 (a) illustrates the resulting compliance from the hybrid of PPR and NPR base materials with optimized macro and micro topologies inserted. From Fig. 14(a), it is known that the resulting compliance decreases with the increment of $\kappa_{\lim}$. When $\kappa_{\lim}$ =2, the resulting compliance lies between the values from exclusive base material 1 and 2. However, the resulting stiffness is enhanced when $\kappa_{\lim}$ equals 2.5, 3.0 and 3.5. Furthermore, it is observed in Fig. 14(a) that the macro and micro structures respectively present distinct topologies under various $\kappa_{\lim}$. For illustrating the stiffness enhancement is not caused by the variations of topological configurations, the optimized results from two PPR base materials, i.e., $v^{(1)} = v^{(2)}$ =0.35, are given in Fig. 14(b). In Fig. 14(b), it is obvious that although the macro and micro structures have the similar topological configurations as shown in Fig. 14(a), the resulting compliance from two PPR base materials always lies between the values of exclusive base material 1 and 2. That is to say the stiffness enhancement is induced by Poisson's ratio effect. The above analysis illustrates that besides NPR and volume fractions of the base materials, the thermal insulation constraint can also influence the Poisson's ratio effect in concurrent structure.
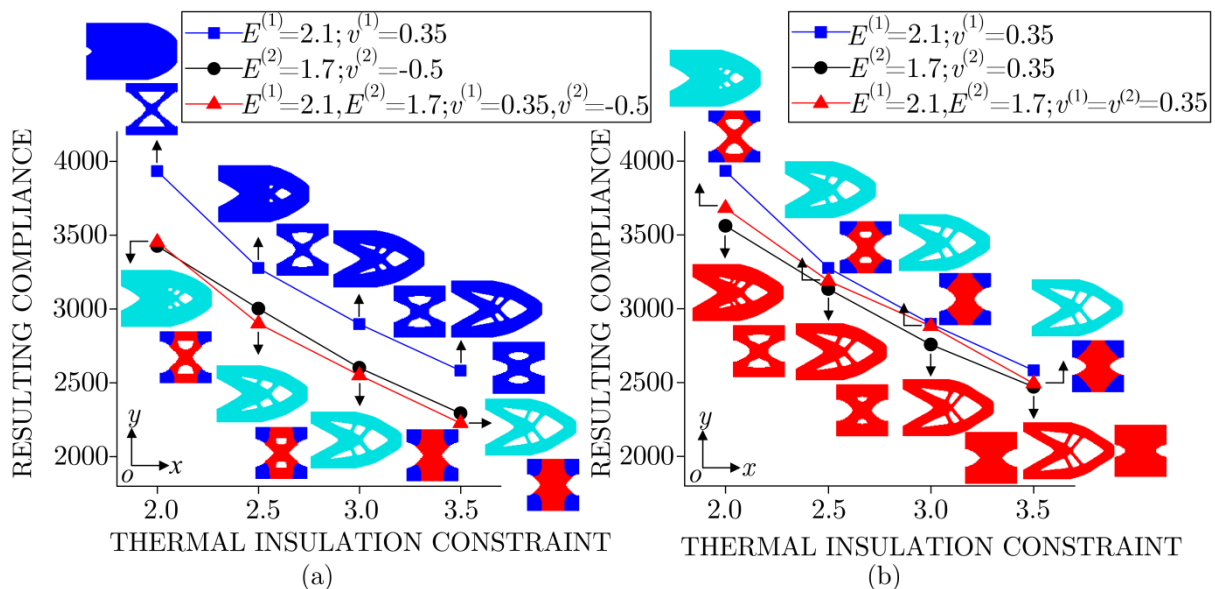

Figure 14: *The influence of the thermal insulation constraint on the resulting compliance:*

(a) hybrid of PPR and NPR base materials (b) hybrid of two PPR base materials.

The trends of f^{mac}, $f^{\mathrm{mic,b}}$, $f^{\mathrm{mic,b1}}$ and $f^{\mathrm{mic,b2}}$ under various $\kappa_{\lim}$ are shown in Fig. 15. From Fig. 15, it can be seen that with increasing of $\kappa_{\lim}$, f^{mac} decreases, $f^{\mathrm{mic,b}}$, $f^{\mathrm{mic,b1}}$ and $f^{\mathrm{mic,b2}}$ increase. This is because f^{b} is fixed, with the increment of $\kappa_{\lim}$, more base materials are demanded on micro-scale, i.e., $f^{\mathrm{mic,b1}}$ and $f^{\mathrm{mic,b2}}$ increase, which results in f^{mac} presenting a decline trend. Moreover, a relative smaller f^{b1} (only 20%) gives rise to $f^{\mathrm{mic,b1}} < f^{\mathrm{mic,b2}}$.
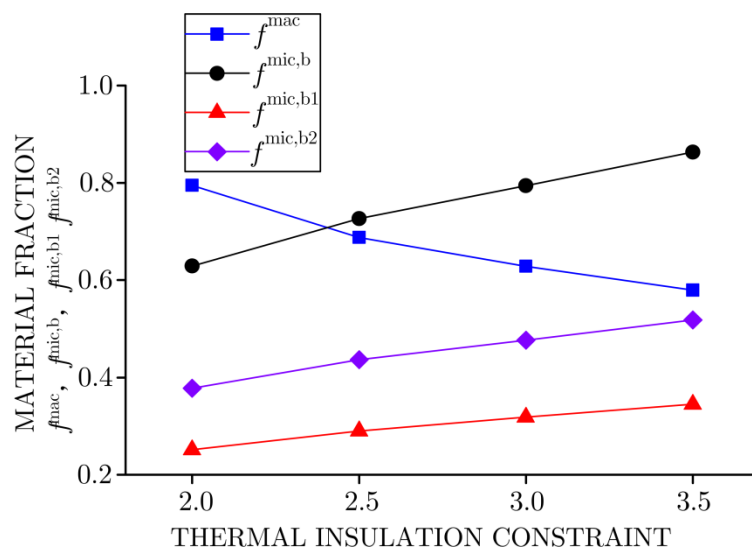
Figure 15: *The influence of* $\kappa_{\lim}$ *on* f^{mac}, $f^{\mathrm{mic,b}}$, $f^{\mathrm{mic,b1}}$ *and* $f^{\mathrm{mic,b2}}$.

6 Conclusion

Respective interpolation scheme of Young's modulus and Poisson's ratio can realize the optimization with distinct Poisson's ratios. Taken the minimized structural compliance as the objective, two optimization problems with different types of constraints are proposed to reveal the Poisson's ratio effect (stiffness enhancement) in concurrent structure. In Problem A, the independent volume fraction constraints are applied on macrostructure and microstructure. In Problem B, besides building the coupled volume relationships between macrostructure and microstructure, the thermal insulation constraint is also considered on micro-scale. Several typical numerical examples clearly demonstrate that the hybrid of PPR and NPR base materials on micro-scale can improve the stiffness of concurrent structure. More conclusions can be obtained as follows

(1) In both Problem A and B, the stiffness of the concurrent structure can be constantly enhanced with the difference between the Poisson's ratios of the base materials increasing.

(2) The resulting compliance varies with the volume fractions of base materials. Moreover, the volume fraction ranges whose objective values can simultaneously exceed the results of exclusive PPR and NPR base materials are gradually enlarged with decreasing of NPR. In Problem A, the optimal proportion of base materials tends to reduce the dosages of PPR base material in microstructure with the decrement of NPR. However, the optimal volume fraction in Problem B does not change with the variation of NPR. Moreover, in Problem B, the macrostructure strongly interacts with microstructure, e.g., with continuously increasing the volume fraction of base material 1, the volume fractions of macrostructure and microstructure respectively increase and decrease monotonically.

(3) When relaxing the thermal insulation requirement, the resulting compliance decreases monotonically. Similar as the volume faction constraint in Problem B, the thermal insulation constraint significantly influences the dosages of base materials between macro and micro scales, e.g., with gradually relaxing the thermal insulation constraint, the volume fractions of macrostructure and microstructure respectively decrease and increase monotonically.

References

Andreassen, E., Andreasen, C. S., (2014). How to determine composite material properties using numerical homogenization. Computational Materials Science 83: 488-95.

Bendsøe, M. P., (1989). Optimal shape design as a material distribution problem. Structural Optimization 1 (4): 193-202.

Bendsøe, M. P., Kikuchi, N., (1988). Generating optimal topologies in structural design using a homogenization method. Computer Methods in Applied Mechanics and Engineering 71 (2): 197-224.

Bourdin, Blaise, Chambolle, Antonin, (2003). Design-dependent loads in topology optimization. Esaim Control Optimisation & Calculus of Variations 9 (9): 19-48.

Da, D. C., Cui, X. Y., Long, K., Li, G. Y., (2017). Concurrent topological design of composite structures and the underlying multi-phase materials. Computers and Structures 179: 1-14.

de Kruijf, N., Zhou, S. W., Li, Q., Mai, Y. W., (2007). Topological design of structures and composite materials with multiobjectives. International Journal of Solids and Structures 44 (22-23): 7092-109.

Deng, J. D., Yan, J., Cheng, G. D., (2013). Multi-objective concurrent topology optimization of thermoelastic structures composed of homogeneous porous material. Structural and Multidisciplinary Optimization 47 (4): 583-97.

Guo, X., Zhang, W. S., Zhong, W. L., (2014). Doing Topology Optimization Explicitly and Geometrically-A New Moving Morphable Components Based Framework. Journal of Applied Mechanics 81 (8): 081009.

Hassani, B., Hinton, E., (1998). A review of homogenization and topology optimization I-homogenization theory for media with periodic structure. Computers and Structures 69 (6): 707-17.

Haug, E. J., Choi, K. K., Komkov, V. 1986. Design Sensitivity Analysis of Structural Systems. Orlando: Academic Press.

Jia, J., Cheng, W., Long, K., (2017). Concurrent design of composite materials and structures considering thermal conductivity constraints. Engineering Optimization: 49(8):1335-53.

Kocer, C., McKenzie, D. R., Bilek, M. M., (2009). Elastic properties of a material composed of alternating layers of negative and positive Poisson's ratio. Materials Science and Engineering A 505 (1-2): 111-5.

Lakes, R., (1993). Materials with structural hierarchy. Nature 361 (6412): 511-5.

Lim, T. C., (2010). In-Plane Stiffness of Semiauxetic Laminates. Journal of Engineering Mechanics 136 (9): 1176-80.

Liu, B., Zhang, L. X., Gao, H. J., (2006). Poisson ratio can play a crucial role in mechanical properties of biocomposites. Mechanics of Materials 38 (12): 1128-42.

Liu, L., Yan, J., Cheng, G. D., (2008). Optimum Structure with Homogeneous Optimum Truss-like Material. Computers and Structures 86 (13-14): 1417-25.

Liu, S. T., Cheng, G. D., Gu, Y., Zheng, X. G., (2002). Mapping method for sensitivity analysis of composite material property. Structural and Multidisciplinary Optimization 24 (3): 212-7.

Long, K., Du, X., Xu, S. Q., Xie, Y. M., (2016). Maximizing the effective Young's modulus of a composite material by exploiting the Poisson effect. Composite Structures 153: 593-600.

Long, K., Han, D., Gu, X. G., (2017). Concurrent topology optimization of composite macrostructure and microstructure constructed by constituent phases of distinct Poisson's ratios for maximum frequency. Computational Materials Science 129: 194-201.

Long, K., Wang, X., Gu, X. G. (2018), Concurrent topology optimization for minimization of total mass considering load-carrying capabilities and thermal insulation simultaneously. Acta Mechanica Sinica 34(2): 315-26.

Long, K., Yuan, P. F., Xu, S. Q., Xie, Y. M (2018)., Concurrent topological design of composite structures and materials containing multiple phases of distinct Poisson's ratios. Engineering Optimization 50(4): 599-614

Mlejnek, H. P., (1992). Some aspects of the genesis of structures. Structural and Multidisciplinary Optimization 5 (1): 64-9.

Niu, B., Yan, J., Cheng, G. D., (2009). Optimum structure with homogeneous optimum cellular material for maximum fundamental frequency. Structural and Multidisciplinary Optimization 39 (2): 115-32.

Querin, O. M., Young, V., Steven, G. P., Xie, Y. M., (2000). Computational efficiency and validation of bi-directional evolutionary structural optimisation. Computer Methods in Applied Mechanics and Engineering 189 (2): 559-73.

Rodrigues, H., Guedes, J. M., Bendsoe, M. P., (2002). Hierarchical optimization of material and structure. Structural and Multidisciplinary Optimization 24 (1): 1-10.

Shufrin, I., Pasternak, E., Dyskin, A. V., (2015). Hybrid materials with negative Poisson's ratio inclusions. International Journal of Engineering Science 89: 100-20.

Sigmund, O., (1997). On the design of compliant mechanisms using topology optimization. Mechanics of Structures and Machines 25 (4): 493-524.

Sigmund, O., (2001). Design of multiphysics actuators using topology optimization-Part II: Two-material structures. Computer Methods in Applied Mechanics and Engineering 190 (49-50): 6605-27.

Sigmund, O., Maute, K., (2013). Topology optimization approaches. Structural and Multidisciplinary Optimization 48 (6): 1031-55.

Sivapuram, R., Dunning, P. D., Kim, H. A., (2016). Simultaneous material and structural optimization by multiscale topology optimization. Structural and Multidisciplinary Optimization 54 (5): 1267-81.

Strek, T., Jopek, H., Maruszewski, B. T., Nienartowicz, M., (2014). Computational analysis of sandwich-structured composites with an auxetic phase. Physica Status Solidi 251: 354–66.

Svanberg, K., (1987). The method of moving asymptotes-a new method for structural optimization. International Journal for Numerical Methods in Engineering 24 (2): 359-73.

Vicente, W. M., Zuo, Z. H., Pavanello, R., Calixto, T. K. L., Picelli, R., Xie, Y. M., (2016). Concurrent topology optimization for minimizing frequency responses of two-level hierarchical structures. Computer Methods in Applied Mechanics and Engineering 301: 116-36.

Wang, M. Y., Wang, X. M., Guo, D. M., (2003). A level set method for structural topology optimization. Computer Methods in Applied Mechanics and Engineering 192 (1–2): 227-46.

Xia, L., Breitkopf, P., (2014). Concurrent topology optimization design of material and structure within FE2 nonlinear multiscale analysis framework. Computer Methods in Applied Mechanics and Engineering 278: 524-42.

Xie, Y. M., Steven, G. P., (1993). A simple evolutionary procedure for structural optimization. Computers and Structures 49 (5): 885-96.

Xu, B., Jiang, J. S., Xie, Y. M., (2015). Concurrent design of composite macrostructure and multi-phase material microstructure for minimum dynamic compliance. Composite Structures 128: 221-33.

Xu, B., Xie, Y. M., (2015). Concurrent design of composite macrostructure and cellular microstructure under random excitations. Composite Structures 123: 65-77.

Xu, B., Huang, X. D., Zhou, S. W., Xie, Y. M., (2016). Concurrent topological design of composite thermoelastic macrostructure and microstructure with multi-phase material for maximum stiffness. Composite Structures 150: 84-102.

Yan, J., Cheng, G. D., Liu, L., (2008). A Uniform Optimum Material Based Model for Concurrent Optimization of Thermoelastic Structures and Materials. International Journal for Simulation and Multidisciplinary Design Optimization 2 (4): 259-66.

Yan, J., Hu, W. B., Duan, Z. Y., (2015). Structure/Material concurrent optimization of lattice materials based on Extended Multiscale Finite Element Method. International Journal for Multiscale Computational Engineering 13 (1): 73-90.

Yan, X. L., Huang, X. D., Zha, Y., Xie, Y. M., (2014). Concurrent topology optimization of structures and their composite microstructures. Computers and Structures 133: 103-10.

Zhang, W. H., Sun, S. P., (2006). Scale-related topology optimization of cellular materials and structures. International Journal for Numerical Methods in Engineering 68 (9): 993-1011.

Zhou, M., Rozvany, G. I. N., (1991). The COC algorithm, Part II: Topological, geometrical and generalized shape optimization. Computer Methods in Applied Mechanics and Engineering 89 (1–3): 309-36.

Zhou, S., Cadman, J., Chen, Y., Li, W., Xie, Y. M., Huang, X., Appleyard, R., Sun, G., Li, Q., (2012). Design and fabrication of biphasic cellular materials with transport properties–A modified bidirectional evolutionary structural optimization procedure and MATLAB program. International Journal of Heat and Mass Transfer 55 (25–26): 8149-62.

Zuo, Z. H., Xie, Y. M., (2014). Maximizing the effective stiffness of laminate composite materials. Computational Materials Science 83 (2): 57–63.